Power flow associated with the Goos-Hänchen shift of a normally incident electromagnetic beam reflected off an antiferromagnet

F. Lima,[1,2] T. Dumelow,[2,3,*] E. L. Albuquerque,[2] and J. A. P. da Costa[3,4]
[1]*Escola Agrícola de Jundaí, Universidade Federal do Rio Grande do Norte, RN 106, Km 03, Distrito de Jundaí, Macaiba 59280-000, RN, Brazil*
[2]*Departamento de Física, Universidade Federal do Rio Grande do Norte, Natal 59072-970, RN, Brazil*
[3]*Departamento de Física, Universidade do Estado do Rio Grande do Norte, Costa e Silva, Mossoró 59610-090, RN, Brazil*[†]
[4]*Departamento de Física, Universidade Federal do Ceará, Campus Pici, Fortaleza 60455-900, CE, Brazil*
(Received 8 January 2009; revised manuscript received 5 April 2009; published 30 April 2009)

We investigate the predicted lateral shift of a normally incident electromagnetic beam upon reflection off an antiferromagnet in an external magnetic field in terms of power flow. In the absence of damping, there is power flow along the interface in the reststrahl regions, even at normal incidence, and this leads directly to a shift similar to the Goos-Hänchen shift normally associated with oblique incidence radiation. In the bulk regions, such a shift is still possible even without this type of power flow. In this case the beam transmitted into the antiferromagnet is displaced in the direction opposite to that of the reflected beam, thus ensuring overall flux continuity.

DOI: 10.1103/PhysRevB.79.155124 PACS number(s): 78.20.Ls, 71.36.+c, 42.25.Bs

I. INTRODUCTION

The lateral displacement of a finite electromagnetic beam reflected at an interface was first observed experimentally by Goos and Hänchen[1] in 1947, and such shifts are usually referred to as Goos-Hänchen shifts. In the past, they were mainly associated with total internal reflection,[2] but this does not need not to be the case. In fact, simple oblique incidence reflection off a metal involves some sort of Goos-Hänchen shift, and this shift may be positive or negative according to the polarization of the incident beam.[3–5] Other examples include reflections off weakly absorbing dielectric[3,6] and double negative[7] media, strongly absorbing media,[8] and photonic crystals.[9] Furthermore, we have predicted that, at frequencies close to the magnon resonances, a Goos-Hänchen shift associated with external reflection off an antiferromagnet should be possible even at normal incidence.[10]

There are several ways of interpreting Goos-Hänchen shifts, including use of the modified plane wave reflection model of Lotsch,[11] the ray optics models of Kogelnik and Weber[12] and of Snyder and Love,[13] and the quantum model of Agudín.[14] Here we highlight two approaches that are especially useful in the present study.

The first approach is to consider any incident beam as made up of a series of plane waves, each with a slightly different incident angle so that if the phase change upon reflection is angular dependent, there will be mutual interference between the reflected waves. This interference manifests itself as a lateral displacement of the reflected beam.[15–17] A particularly satisfying version of this approach is the angular spectrum model[16] in the form expressed by McGuirk and Carniglia.[17] This method employs a full integral of all the plane waves making up the incident beam yet is able to predict the Goos-Hänchen shift in a very simple way.

The second approach is to consider energy conservation using the model of Renard.[18] If there is energy flow along the interface, as occurs when evanescent waves are excited in the second medium due to obliquely incident radiation in the first, energy conservation requires that the reflected beam be displaced along the surface in the same direction as the energy flow. A detailed analysis of energy flow in the case of reflection of a Gaussian beam is given by Lai *et al.*[19]

In our previous report on the normal incidence Goos-Hänchen shift,[10] the results were interpreted using an angular spectrum model based on that of McGuirk and Carniglia.[17] This model shows that nonreciprocity in the phase of the reflected radiation is necessary to induce such a shift. This type of nonreciprocity should indeed exist in the case of external reflection off an antiferromagnet in the presence of an external magnetic field.[20] It may occur both within the reststrahl frequency regions, for which reflection is total (ignoring damping), and in the bulk frequency regions, for which a proportion of the incident radiation propagates into the sample. A normal incidence Goos-Hänchen shift is therefore predicted in both types of region. In the present paper we study the power flow associated with such a shift.

In the traditional power conservation model of Renard,[18] Goos-Hänchen shifts are associated with energy flow, via evanescent fields, along the interface. In the present case of normal incidence reflection off an antiferromagnet, such evanescent fields exist in the reststrahl regions but not in the bulk regions. A full understanding of the associated Goos-Hänchen shift therefore requires a detailed analysis of the power flow both at reststrahl region and at bulk region frequencies, and this is the aim of the present work.

The plan of the paper is as follows. In Sec. II we examine power flow associated with a plane wave normally incident on an antiferromagnet in the presence of an external magnetic field and derive expressions for the direction of power flow within the antiferromagnet. In Sec. III we use these results to model the lateral shift in the reststrahl regions, ignoring damping, of a finite incident beam, using energy conservation principles. Section IV then compares these results with those of the angular spectrum model used in the previous paper.[10] In Sec. V we examine the energy flux as-

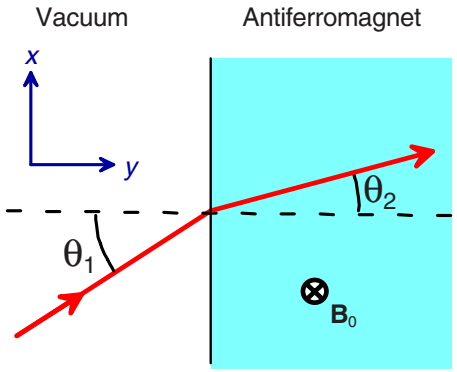

FIG. 1. (Color online) Geometry considered in this paper. The arrows represent the direction of power flow (Poynting vector).

sociated with reflection of a normally incident Gaussian beam, comparing the behavior in reststrahl regions to that in the bulk regions. For most of the analysis we ignore damping so that we can directly follow the flux lines in a manner similar to that employed by Lai *et al.*,[19] but we nevertheless briefly discuss the effect of damping on the power flow. Finally, in Sec. VI we offer some overall conclusions.

II. POWER FLOW ON PLANE WAVE REFLECTION OFF AN ANTIFERROMAGNET

We first consider the power flow associated with plane wave reflection off a semi-infinite antiferromagnet in the Voigt geometry. Although the main purpose of this section is to derive expressions for power flow resulting from normally incident radiation, we do not restrict the analysis in this section to normal incidence. This is because, in the later part of the paper, we use some of the intermediate results obtained for nonzero incident angles in the angular spectrum analysis of Goos-Hänchen shifts and in the simulation of the reflection of Gaussian beams.

The basic geometry is shown in Fig. 1. We consider *s*-polarized incident radiation whose electric field contribution lies along the z axis. The plane of incidence is xy, with the y axis normal to the sample surface. The anisotropy axis of the antiferromagnet is along z, and an external field $\mathbf{B}_0$ also lies along this direction.

The magnetic permeability tensor of an antiferromagnet, having both its anisotropy field and an external field directed along the z axis, is given, at frequency ω, by[21]

$$\mu = \begin{pmatrix} \mu_1 & i\mu_2 & 0 \\ -i\mu_2 & \mu_1 & 0 \\ 0 & 0 & 1 \end{pmatrix}, \tag{1}$$

where

$$\mu_1 = 1 + \mu_0 \gamma^2 B_A M_S (Y^+ + Y^-), \tag{2a}$$

$$\mu_2 = \mu_0 \gamma^2 B_A M_S (Y^+ - Y^-), \tag{2b}$$

$$Y^{\pm} = [\omega_r^2 - (\omega \pm \gamma B_0 + i\Gamma)^2]^{-1}. \tag{2c}$$

Here B_A is the anisotropy field, M_S is the sublattice magnetization, γ is the gyromagnetic ratio, and Γ is the damping parameter. ω_r is the zero-field magnetic resonance frequency given by

$$\omega_r = \gamma(2B_A B_E + B_A^2)^{1/2}, \tag{3}$$

where B_E is the exchange field. From the above equations, we see that the permeability tensor is diagonal ($\mu_2 = 0$) in the absence of an external field, but the antiferromagnet becomes gyromagnetic ($\mu_2 \neq 0$) if B_0 is nonzero. This is the source of the effects studied in the present paper.

We first consider the wave vectors in the two media shown in Fig. 1. The in-plane component is the same in both media and is given by

$$k_x = k_0 \sin\theta_1, \tag{4}$$

where $k_0 = \omega/c$ and θ_1 is the angle of incidence. The y components in layers 1 and 2 are given by[22]

$$k_{1y} = [k_0^2 - k_x^2]^{1/2}, \tag{5a}$$

$$k_{2y} = [\epsilon\mu_v k_0^2 - k_x^2]^{1/2}, \tag{5b}$$

respectively, where ϵ is the dielectric constant of the antiferromagnet and μ_v is its Voigt permeability given by

$$\mu_v = (\mu_1^2 - \mu_2^2)/\mu_1. \tag{6}$$

The complex reflection coefficient is given by[22]

$$r = \frac{k_{1y}\mu_v - k_{2y} - ik_x(\mu_2/\mu_1)}{k_{1y}\mu_v + k_{2y} + ik_x(\mu_2/\mu_1)}, \tag{7}$$

with overall reflectivity $R = rr^*$. The complex reflection coefficient, in terms of the electric field, is simply $1+r$, giving

$$t = \frac{2k_{1y}\mu_v(\mu_2/\mu_1)}{k_{1y}\mu_v + k_{2y} + ik_x(\mu_2/\mu_1)}. \tag{8}$$

We now turn to the power flow itself, as represented by the time-averaged Poynting vector,[23]

$$\langle \mathbf{S} \rangle = 1/2\ \mathrm{Re}(\mathbf{E} \times \mathbf{H}^*). \tag{9}$$

In the Voigt geometry, the $\mathbf{E}$ field is confined along the z axis, so the Poynting vector is most easily represented in terms of the E_z field, making use of the conversion $\mathbf{k} \times \mathbf{E} = \omega\mu_0\mu\mathbf{H}$. The resulting time-averaged Poynting vector has components

$$\langle S_{2x} \rangle = \frac{|E_z|^2}{2\omega\mu_0} \mathrm{Re}\left[\frac{k_x - ik_{2y}(\mu_2/\mu_1)}{\mu_v}\right], \tag{10a}$$

$$\langle S_{2y} \rangle = \frac{|E_z|^2}{2\omega\mu_0} \mathrm{Re}\left[\frac{k_{2y} + ik_x(\mu_2/\mu_1)}{\mu_v}\right]. \tag{10b}$$

The direction of power flow, or angle of refraction, marked as θ_2 in Fig. 1, is given by $\tan\theta_2 = \langle S_{2x} \rangle / \langle S_{2y} \rangle$. Here we analyze this angle with particular reference to normal incidence reflection (corresponding to $k_x = 0$) off MnF_2 at 4.2 K, in an external magnetic field $\mathbf{B}_0$ of magnitude 0.1 T. For this material, the relevant parameters are:[24] $M_S = 6.0 \times 10^5$ A/m, $B_A = 0.787$ T, $B_E = 53.0$ T, and $\gamma = 0.975$ cm^{-1}/T, corresponding to $\omega_r = 8.94$ cm^{-1}. The

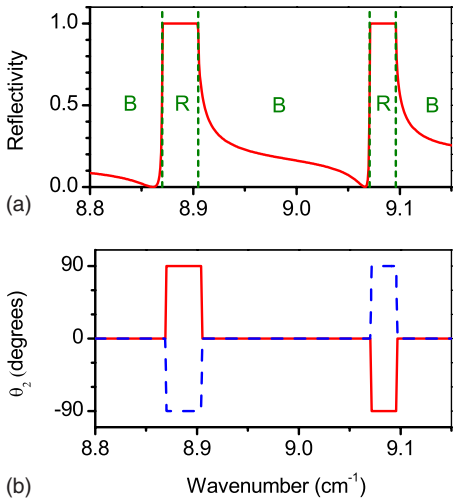

FIG. 2. (Color online) Calculated normal incidence (a) reflectivity and (b) θ_2 values upon reflection off MnF_2 in a field of $B_0 = \pm 0.1$ T, assuming $\Gamma = 0$, as a function of frequency (expressed as wave number $\omega/2\pi c$). In (b) the solid red line is for $B_0 = +0.1$ T and the blue dashed line is for $B_0 = -0.1$ T. The vertical dashed lines in (a) separate the bulk regions (marked as B) from those of reststrahl regions (marked as R).

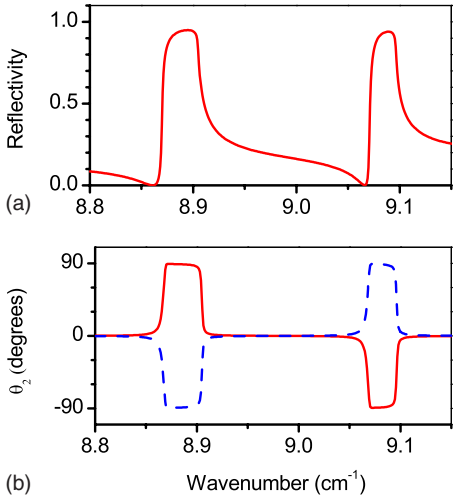

FIG. 3. (Color online) Calculated normal incidence (a) reflectivity and (b) θ_2 values upon reflection off MnF_2 in a field of $B_0 = \pm 0.1$ T, assuming $\Gamma = 0.0007$ cm^{-1}. In (b) the solid red line is for $B_0 = +0.1$ T and the blue dashed line is for $B_0 = -0.1$ T.

damping factor is $\Gamma = 0.0007$ cm^{-1} and the dielectric constant is $\epsilon = 5.5$.

We restrict ourselves initially to the idealized case where there is no damping in the system, i.e., $\Gamma = 0$. In this case, μ_1, μ_2, and μ_v are all wholly real, and k_{2y} can be either wholly real or wholly imaginary. Equation (5) shows that, at normal incidence ($k_x = 0$ or $\theta_1 = 0$), k_{2y} is real in regions where μ_v is positive (the bulk regions) and imaginary in regions where μ_v is negative (the reststrahl regions). In the former case radiation will propagate into the sample, but in the latter case it will be wholly reflected, with an evanescent field within the sample decaying away from the surface. The effect on the reflectivity spectra is shown in Fig. 2(a). The regions for which $R < 1$ are the bulk regions (marked B in the figure) corresponding to k_{2y} real. The regions of total reflection, $R = 1$, are the reststrahl regions (marked R in the figure), with k_{2y} imaginary.

Inspection of Eq. (10) shows that in general, for $k_x = 0$, $\langle S_{2x} \rangle$ will be zero and $\langle S_{2y} \rangle$ nonzero for k_{2y} real (bulk regions), whereas the converse will be true for k_{2y} imaginary (reststrahl regions). Thus $\theta_2 = 0$ in the bulk regions, corresponding to power flow normal to the surface, and $\theta_2 = \pm 90°$ in the reststrahl regions, corresponding to energy flow parallel to the surface, as shown in Fig. 2(b). The direction of energy flow parallel to the surface in the reststrahl regions depends on the sign of B_0 (using the notation of Fig. 1) since this determines the sign of μ_2.

The possibility of power flow parallel to the surface at normal incidence, which appears somewhat counterintuitive, can be interpreted as follows. Field continuity requires that the B_y component of the electromagnetic field be the same on both sides of the interface. Clearly, at normal incidence, B_y is zero in the vacuum layer so that it must also be zero in the antiferromagnet, immediately to the right of the interface. Writing this field in terms of the **H** field components in the antiferromagnet, we get

$$B_y/\mu_0 = -i\mu_2 H_x + \mu_1 H_y = 0. \tag{11}$$

In general μ_1 is nonzero so that, if μ_2 is also nonzero (i.e., $B_0 \neq 0$), the **H** field will have both x and y components within the antiferromagnet, with a phase difference of $\pi/2$ between the two components. In practice the oscillating **E** field (whose only component is E_z) is in phase (or in antiphase) with one of these **H** field components and in quadrature with the other one. In the bulk regions E_z is in phase with H_x and in quadrature with H_y, so only the E_z and H_x field components contribute to the power flow. The Poynting vector, and thus the direction of power flow, is perpendicular to these field components along y (i.e., normal to the interface). In the reststrahl regions, in contrast, E_z is in quadrature with H_x and either in phase or in antiphase with H_y, depending on the sign of μ_2. The power flow direction is now perpendicular to the E_z and H_y components along $\pm x$ (i.e., parallel to the interface). This power flow is associated with the evanescent fields within the antiferromagnet, and thus its intensity decays away from the interface.

In the presence of damping (Γ nonzero), k_{2y} becomes complex, and there is no distinct division between bulk and reststrahl regions, as seen from the reflectivity spectrum in Fig. 3(a). θ_2 is thus no longer restricted to zero or $\pm 90°$. This is seen from Fig. 3(b), which shows that there is now a continuous variation in θ_2 with frequency.

III. LATERAL SHIFT OF A REFLECTED BEAM DUE TO POWER FLOW ALONG THE INTERFACE

As discussed in the previous section, at frequencies corresponding to the reststrahl regions, normally incident plane wave radiation induces power flow, within the antiferromagnet, along the vacuum/antiferromagnet interface. This suggests that there should be a corresponding lateral displacement, similar to the Goos-Hänchen shift, of a finite beam upon reflection. In this section we consider how the power

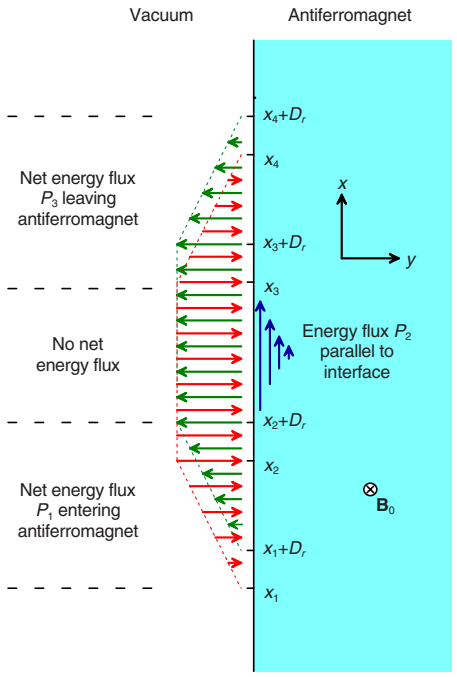

FIG. 4. (Color online) Model of lateral displacement of reflected beam in the reststrahl regions in terms of power flow along the antiferromagnet surface.

flow associated with the evanescent wave in the antiferromagnet induces such a shift. Our model, which investigates the shift in the wide beam limit, is similar to that employed by Renard[18] to describe the classical Goos-Hänchen shift on total internal reflection.

If the incident beam is sufficiently wide, there will be a central portion of the beam which can be considered as a plane wave of constant intensity. At either side of this central portion the intensity will gradually decrease to zero. This is represented schematically in Fig. 4. In this figure the central portion of constant intensity lies between x_2 and x_3, with the intensity decaying to zero between x_2 and x_1 and between x_3 and x_4. Obviously in practice the positions of x_1, x_2, x_3, and x_4 are not as distinct as shown in the figure, but this does not affect the general model. We consider the case of zero damping for which we must have conservation of energy flow. The plane wave portion of the beam between x_2 and x_3 will follow the behavior described in the previous section, so, at reststrahl frequencies, there should be a corresponding energy flux P_2 (assumed positive in the figure) parallel to the interface within the antiferromagnet. Conservation of energy flux therefore requires that there must be a net flux P_1 entering in the region near one edge of the beam and a net flux P_3 leaving the surface in the region near the other. This is equivalent to a lateral shift D_r of the reflected beam with respect to the incident beam. Thus P_1 enters in the region between x_1 and x_2+D_r and P_3 leaves in the region between x_3 and x_4+D_r. In the region between x_2+D_r and x_3 the incident and reflected fluxes cancel, so the net flux is zero.

We consider energy flow within a slice, of thickness Δz, in the xy plane. Since all energy flows occur in the xy plane, there must be energy conservation within this slice, i.e., $P_1=P_2=P_3$. From Fig. 4, one can see that the net flux P_1 entering at the lower edge of the incident beam is given by

$$P_1 = \int_{x_1}^{x_2} \langle S_i(x)\rangle \Delta z dx + \int_{x_2}^{x_2+D_r} \langle S_i(x)\rangle \Delta z dx + \int_{x_1+D_r}^{x_2+D_r} \langle S_r(x)\rangle \Delta z dx, \tag{12}$$

where $\langle S_i(x)\rangle$ and $\langle S_r(x)\rangle$ are a measure of the local intensities, represented in terms of time-averaged Poynting vectors along y of the incident and reflected waves, respectively. Now, assuming that the shape of the reflected beam is the same as that of the incident beam (the validity of this assumption will be verified using the angular spectrum model in the next section), we have

$$\langle S_i(x)\rangle = -\langle S_r(x+D_r)\rangle \tag{13}$$

so that the first and last terms on the right-hand side of Eq. (12) cancel. The remaining integral is performed within the range from x_2 to x_2+D_r, corresponding to the central portion of the incident beam. In this region the incident time-averaged Poynting vector is maximum and has a constant value $\langle S_{\max}\rangle$. Equation (12) thus reduces to

$$P_1 = \langle S_{\max}\rangle \Delta z D_r, \tag{14}$$

where $\langle S_{\max}\rangle$ is given, in terms of the incident field $E_{\max}$ within the central region of the beam, by

$$\langle S_{\max}\rangle = \frac{k_0 |E_{\max}|^2}{2\omega\mu_0}. \tag{15}$$

Within the antiferromagnet, the overall energy flux P_2 along x is given by

$$P_2 = \int_0^\infty \langle S_{2x}(y)\rangle \Delta z dy, \tag{16}$$

where we take $y=0$ to be at the surface of the antiferromagnet. Now P_2 is simply the flux parallel to the surface due to a normally incident plane wave of intensity $\langle S_{\max}\rangle$. $\langle S_{2x}(y)\rangle$ is therefore given by Eq. (10) with $k_x=0$ and E_z equal to

$$E_z(y) = tE_{\max} \exp(ik_{2y}y). \tag{17}$$

In the above, k_{2y} is obtained from Eq. (5) and t from Eq. (8).

Making the appropriate substitutions into Eqs. (14) and (16) and putting $P_1=P_2$, we get, after some algebra,

$$D_r = \frac{2(\mu_2/\mu_1)}{k_0(\mu_v - \epsilon)}. \tag{18}$$

Thus we see that, in the absence of absorption, simple energy conservation principles may be used to predict a lateral shift of the reflected beam at frequencies within the reststrahl regions. This shift displays distinct nonreciprocal behavior associated with the presence of the static field $\mathbf{B}_0$. Thus, if we were to imagine a reversal in the direction of the reflected beam in Fig. 4, so that it became a new incident beam, we would see that the energy would not return along its original path. Instead, within the antiferromagnet, it would travel in the positive x direction, thus causing a further positive shift D_r in the new reflected beam. If, on the other hand, the

direction of $\mathbf{B}_0$ was also reversed, the energy within the antiferromagnet would travel in the negative x direction and would once again trace its original path.

IV. ANGULAR SPECTRUM MODEL OF THE LATERAL SHIFT

The energy conservation analysis used in Sec. III to predict the lateral shift D_r, given by Eq. (18), assumes total reflection of the incident beam. Thus it is applicable to reflection in the reststrahl regions in the absence of damping. However, in our previous paper,[10] an angular spectrum analysis, similar to that of McGuirk and Carniglia,[17] was used to predict the lateral shift of the reflected beam in both the reststrahl regions and the bulk regions, irrespective of damping. This analysis interprets the lateral shift as essentially an interference effect. Here we summarize the model and compare its results with those predicted in Sec. III. As before, the model is valid or is a sufficiently wide beam.

In the angular spectrum representation, we consider the incident beam as a sum of plane waves of the form

$$E_i(x,y) = \int_{-k_0}^{k_0} \psi(k_x)\exp[i(k_x x + k_{1y} y)]dk_x, \tag{19}$$

where $\psi(k_x)$ is a distribution function representing the shape of the beam. At the sample surface, which we place at $y=0$, the electric field of the incident beam becomes

$$E_i(x,0) = \int_{-k_0}^{k_0} \psi(k_x)\exp(ik_x x)dk_x, \tag{20}$$

with a corresponding reflected beam whose electric field at the surface is given by

$$E_r(x,0) = \int_{-k_0}^{k_0} r(k_x)\psi(k_x)\exp(ik_x x)dk_x. \tag{21}$$

Here $r(k_x)$ represents the complex reflection coefficient for the relevant plane wave component and is given by Eq. (7). It is convenient to consider this complex coefficient in terms of amplitude ρ_r and phase ϕ_r; i.e.,

$$r(k_x) = \rho_r(k_x)\exp[i\phi_r(k_x)]. \tag{22}$$

For a typical beam, there will be a narrow distribution of k_x values. In the case of normal incidence, this distribution will be centered around $k_x=0$. If we expand ρ_r and ϕ_r as a Taylor series around $k_x=0$, it is straightforward to show that, to a good approximation, Eq. (21) can be written as[10]

$$E_r(x) = r(0)\int_{-k_0}^{k_0} \psi(k_x)\exp\left[ik_x\left(x + \left.\frac{d\phi_r}{dk_x}\right|_{k_x=0}\right)\right]dk_x, \tag{23}$$

where $r(0)$ is the normal incidence plane wave reflection coefficient. It is thus seen that the integral that gives the shape of the reflected beam [Eq. (23)] is the same as that for the incident beam [Eq. (20)] except that x has been replaced by $x+d\phi_r/dk_x|_{k_x=0}$; i.e., the reflected beam has been shifted along the surface of the sample by a distance D_r equal to

$$D_r = -\left.\frac{d\phi_r}{dk_x}\right|_{k_x=0}. \tag{24}$$

The above argument shows that a nonzero lateral displacement D_r in the reflected beam at normal incidence requires nonreciprocity in the reflected phase; i.e., $\phi_r(k_x) \neq \phi_r(-k_x)$. The importance of this nonreciprocity can be understood when one notes that the Eq. (21), representing the profile of the reflected field, can be rewritten as

$$E_r(x,0) = \int_0^{k_0} [r(k_x)\psi(k_x)\exp(ik_x x) + r(-k_x)\psi(-k_x)\exp(-ik_x x)]dk_x. \tag{25}$$

We consider the case of a symmetrical incident beam so that $\psi(k_x)=\psi(-k_x)$. Thus, if $r(k_x)=r(-k_x)$ (reciprocal reflection), then $E_r(x,0)=E_r(-x,0)$; i.e., the reflected beam is symmetrical around $x=0$ in the same way as the incident beam. If, however, $r(k_x)$ and $r(-k_x)$ have different phases, then $E_r(x,0) \neq E_r(-x,0)$, amounting to a lateral shift of the reflected beam. The shift can thus be interpreted in terms of the interference between the two terms in the integral of Eq. (25).

A straightforward analysis of Eq. (7) shows that the nonreciprocity condition $\phi_r(k_x) \neq \phi_r(-k_x)$ is satisfied upon reflection off an antiferromagnet in the Voigt geometry.[20] Furthermore, in the absence of damping, the reflection coefficient r can easily be resolved into its real and imaginary parts, allowing explicit evaluation of Eq. (24). This leads exactly to the lateral shift predicted from energy conservation considerations [Eq. (18)] in the reststrahl regions. However, we now find that a shift should also occur at frequencies corresponding to the bulk regions and that such a shift should also be given by Eq. (18). Figure 5(b) shows the shift D_r calculated in both reststrahl and bulk regions close to the upper reststrahl region [Fig. 5(a) shows the reflectivity plot in the same region for comparison]. Nonzero shifts are observed in both regions, with a discontinuity at the reflection minimum, corresponding to $\mu_v=\epsilon$. At frequencies around the lower reststrahl region there is a similar shift but of opposite sign.

In the presence of damping, we can still use Eq. (24), evaluated numerically. However, in practice, the calculated lateral shift is almost identical to that obtained in the absence of damping.[10]

The same argument as used to predict a displacement D_r of the reflected field also predicts a displacement D_t of the field transmitted into the sample. This displacement is thus given by

$$D_t = -\left.\frac{d\phi_t}{dk_x}\right|_{k_x=0}, \tag{26}$$

where ϕ_t is the phase change in the field transmitted across the interface. In the absence of damping this gives

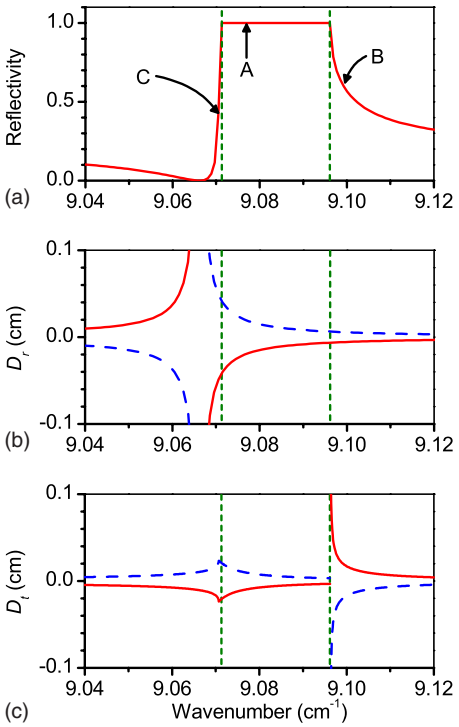

FIG. 5. (Color online) (a) Reflectivity, (b) lateral displacement of reflected field D_r, and (c) lateral displacement of transmitted field D_t as a function of frequency for normal incidence reflection off MnF_2 in an external magnetic field of ± 0.1 T. In (b) and (c) the solid red curves are for $B_0=+0.1$ T and the blue dashed curves are for $B_0=-0.1$ T. The vertical green dashed lines mark the edges of the reststrahl regions. The marked frequencies are A: 9.0769 cm^{-1}; B: 9.0994 cm^{-1}; and C: 9.0705 cm^{-1}.

$$D_t = \frac{(\mu_2/\mu_1)}{k_0(\mu_v - \epsilon)} \tag{27}$$

in the reststrahl regions and

$$D_t = \frac{(\mu_2/\mu_1)}{k_0[\mu_v + (\epsilon\mu_v)^{1/2}]} \tag{28}$$

in the bulk regions.

The variation in D_t with frequency is shown in Fig. 5(c). Note that, although both Eqs. (27) and (28) are obtained directly from Eq. (26), their physical interpretation is rather different. In the case of the reststrahl regions, the field in the antiferromagnet is evanescent, and power flow is along the surface, as discussed in the previous section. The field intensity within the antiferromagnet should be expected to reach a maximum at a position halfway between the maxima of the incident and transmitted beams; i.e., $D_t=D_r/2$. This is exactly what Eq. (27) shows and can be seen graphically by comparing Figs. 5(b) and 5(c) at reststrahl region frequencies.

At bulk region frequencies, a beam propagates into the antiferromagnet normal to the interface. Equation (28) thus represents the lateral displacement of the field associated with this propagating beam with respect to that of the incident beam. For most (but not all) frequencies corresponding to the bulk regions, D_t and D_r have opposite signs; i.e., the lateral displacement of the transmitted field is in the opposite direction to that of the reflected field. This can be best interpreted using the example of a specific beam profile, such as that of a Gaussian beam. This will be done in the following section.

V. ENERGY FLOW ASSOCIATED WITH NORMAL INCIDENCE REFLECTION OF A GAUSSIAN BEAM

From the previous section we see that, in the reststrahl regions, the angular spectrum model is in exact agreement with the result expected from the energy conservation model of Sec. III as long as damping is ignored. However, the angular spectrum model makes further predictions, not covered by the theory of Sec. III, for frequencies outside the reststrahl regions.

In order to investigate energy flow in the reststrahl regions in further detail, and extend the study of energy flow to the bulk regions, we consider the specific case of normal incidence reflection of a Gaussian beam. The basic behavior is analyzed assuming zero damping since we then have zero absorption and thus flux continuity. However, we also briefly discuss the changes that occur when damping is taken into account.

We consider an incident Gaussian beam, focused onto the sample, in the form of Eq. (19) with[16]

$$\psi(k_x) = \frac{g}{2\sqrt{\pi}}\exp\left(-\frac{g^2k_x^2}{4}\right), \tag{29}$$

where $2g$ represents the beam width in the focal plane (the sample surface). At the sample surface the incident beam profile is thus represented by Eq. (20) and the reflected beam profile by Eq. (21). We have, in general, retained the limits of $\pm k_0$ for the integrals since limits of $\pm\infty$, which would give strict Gaussian beams, would involve unrealistically large evanescent fields for $y<0$.[25]

Since the effects are more easily demonstrated for narrow beams, we take $g=\lambda$, the free space wavelength of the radiation used. It should be remembered, however, that the theories of Secs. III and IV both assume wide beams. Nevertheless, provided that the reflectivity is not too small, the theoretical results presented in these sections have, in practice, been found to hold well even for beams as narrow as this.[10]

We consider Gaussian beams at the three frequencies marked as A (9.0769 cm^{-1}), B (9.0994 cm^{-1}), and C (9.0705 cm^{-1}) in Fig. 5(a). We take $B_0=+0.1$ T. At all three frequencies the lateral shift of the reflected beam should be negative, as seen from Fig. 5(b). Frequency A shows the type of behavior expected in the reststrahl regions. The lateral shift of the electric field profile in this case is in the same direction as that of the reflected beam (D_r and D_t have the same sign). Frequency B is representative of most of the bulk region frequencies, with D_r and D_t having opposite signs. Frequency C represents the narrow region between the reflection minimum and the reststrahl region. This is also a bulk region frequency, but in this case D_r and D_t have the same sign.

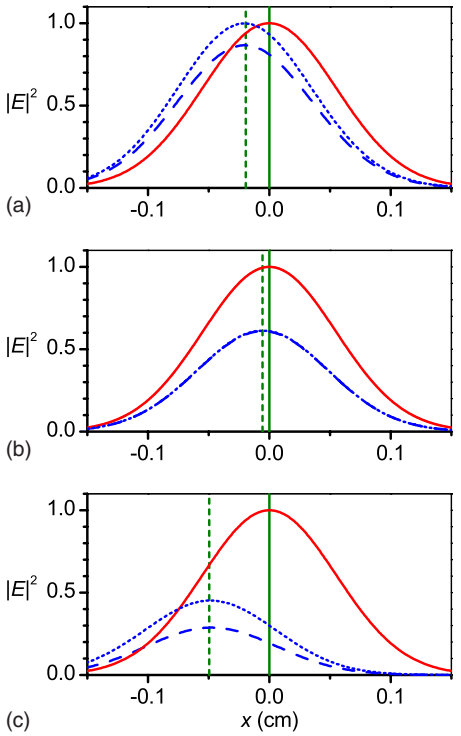

FIG. 6. (Color online) Intensity profiles, along the sample surface, in the case of reflection of a normally incident Gaussian beam, of width $g=\lambda$, off MnF_2 in an external magnetic field of 0.1 T. Solid red curve: incident beam; dotted blue curve: reflected beam in the absence of damping; and dashed blue curve: reflected beams with $\Gamma=0.0007$ cm^{-1}. (a) Frequency A (9.0769 cm^{-1}); (b) frequency B (9.0994 cm^{-1}); and (c) frequency C (9.0705 cm^{-1}). In each case the solid vertical green line at $x=0$ represents the center of the incident beam, and the vertical dashed line represents the center of the reflected beam predicted by Eq. (18). In (b) the reflected intensities with and without damping are almost identical and the curves cannot be separated.

In the incident (vacuum) layer, the beam intensity profiles are well represented by $|E|^2$. The calculated profiles of the incident and reflected beams at the sample surface are shown in Fig. 6, both with and without damping. It can be seen that there is a shift of the reflected beam in excellent agreement with the theoretical result predicted by Eq. (18) (vertical dashed lines) in all cases despite the narrowness of the Gaussian beam used in the simulation. It is also seen that damping has no significant effect on this shift, although in general it reduces the intensity of the reflected beam due to absorption (in the case of frequency B, however, the damped and undamped curves are almost coincident). In the reststrahl region, the beam is totally reflected in the absence of damping but partially absorbed in the presence of damping [Fig. 6(a)]. In the bulk regions, the reflected beam is smaller than the incident beam in all cases.

In order to investigate the power flow in the xy plane we must first calculate the field distribution throughout the plane. The incident electric field profile is given by Eq. (19), with the reflected and transmitted field electric profiles given by

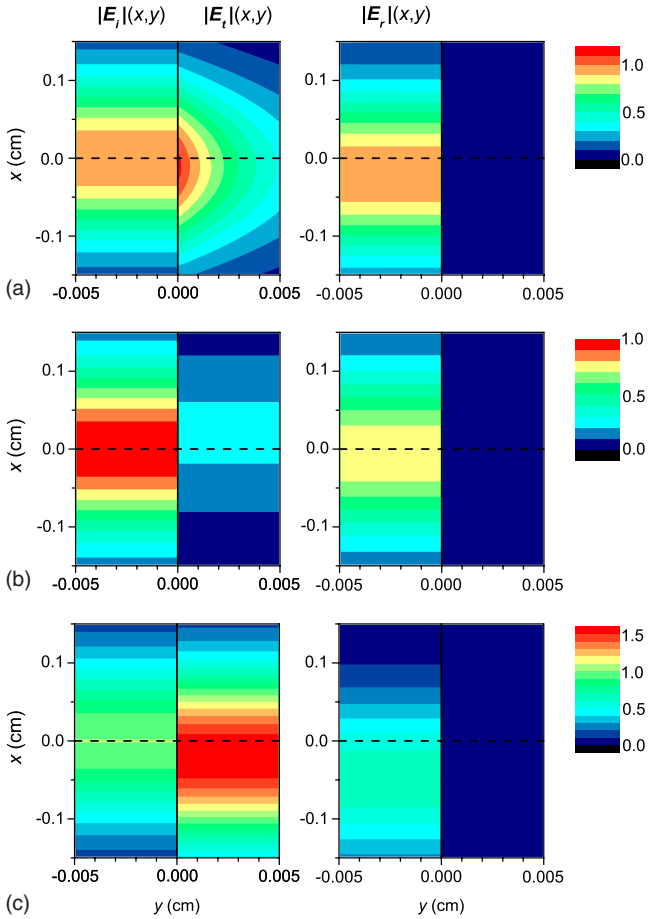

FIG. 7. (Color online) Profiles of the amplitudes of the incident, transmitted, and reflected E fields (E_i, E_t, and E_r, respectively) in the case of reflection of a normally incident Gaussian beam, of width $g=\lambda$, off a semi-infinite sample of MnF_2 in an external magnetic field of 0.1 T, in the absence of damping. (a) Frequency A (9.0769 cm^{-1}); (b) frequency B (9.0994 cm^{-1}); and (c) frequency C (9.0705 cm^{-1}). The solid vertical black line represents the surface of the sample, and the horizontal dashed line at $x=0$ is a guide to the eyes showing the central axis of the incident beam. Note that, for the sake of clarity, the horizontal scale (y) is expanded with respect to the vertical scale (x).

$$E_r(x,y) = \int_{-k_0}^{k_0} r(k_x)\psi(k_x)\exp[i(k_x x - k_{1y} y)]dk_x \qquad (30)$$

and

$$E_t(x,y) = \int_{-k_0}^{k_0} t(k_x)\psi(k_x)\exp[i(k_x x + k_{2y} y)]dk_x, \qquad (31)$$

respectively.

The profiles of the resulting field amplitudes, assuming zero damping, for the three frequencies—A, B, and C—are shown in Fig. 7. In each case the left-hand panel shows both the profile of the incident field E_i (in the region $y<0$) and that of the transmitted field E_t (in the region $y>0$). The right-hand panel shows the profile of the reflected field E_r, displaced along x in the manner already seen in Fig. 6. The transmitted fields are also seen to be displaced as predicted

by Eqs. (27) and (28). The figure also confirms that in the reststrahl regions [Fig. 7(a)] the transmitted field is evanescent, decaying away from the interface, whereas in the bulk regions [Figs. 7(b) and 7(c)] there is no decay in the absence of damping.

In order to calculate the power flow, we also need the magnetic component **H** of the electromagnetic field. This may be obtained at any position in the xy plane by applying $\mathbf{k}\times\mathbf{E}=\omega\mu_0\mu\mathbf{H}$ to each plane wave component in the integrals of Eqs. (19), (30), and (31) and performing the appropriate integration in terms of the **H** field. The time-averaged Poynting vector is then given by Eq. (9). In practice, our main interest is in the overall energy flux, so we calculate the Poynting vector from the overall fields. Thus in the region $y<0$ the Poynting vector is obtained from the sum of the incident and reflected fields, whereas in the region $y>0$, it is obtained from the transmitted field only.

The Poynting vector calculated in this way gives both the power flow intensity and the direction of power flow at each point. This allows us not only to plot the Poynting vector intensity but also, in the absence of absorption, to trace the path of the associated flux lines. This leads to a flux flow pattern analogous to that calculated by Lai *et al.*[19] for the more conventional Goos-Hänchen shift.

We show both the power flow intensity and the flux line pattern in Fig. 8. In each case, the flux lines are calculated as follows. First of all the $\langle S_y\rangle$ values are calculated along the x axis on the left of the figure ($y=-0.005$ cm in this case). Since, at the start of the lines, we are only interested in energy entering from the left, the negative $\langle S_y\rangle$ values are ignored. The integration $\int_{-\infty}^{\infty}\langle S_y\rangle dx$ is then evaluated numerically (in practice using finite limits) over the remaining positive values. In the case of eight flux lines, the start of each line is chosen such that the integration $\int\langle S_y\rangle dx$ between adjacent lines is one-ninth of the overall integral. In this way the line spacing is inversely proportional to the power flow intensity. For each flux line, the direction of power flow at the start of the line is calculated from the time-averaged Poynting vector, and a short (in principle infinitesimal) line is traced along this direction. The end of this line then serves as the new starting point. The power flow direction is once again calculated, and a new short line traced. The process is repeated many times until the whole flux line is traced out.

The power flow pattern at frequency A, in the reststrahl region, is shown in Fig. 8(a). Here the situation is similar to that discussed in Sec. III. For $x\gtrsim -0.01$ cm, in the upper region of the figure, the incident intensity is greater than the reflected intensity [see Fig. 6(a)] so that the overall power flow is to the right. At $x\simeq -0.01$ cm, the incident and reflected beams cancel, whereas for $x\lesssim -0.01$ cm, the reflected beam dominates and the overall power flow is to the left. This behavior is consistent with flux continuity if we have energy flow along the surface within the antiferromagnet in the negative x direction, following the flux line pattern in Fig. 8(a). It is seen that that, since the incident beam is not a single plane wave, the flux lines within the antiferromagnet are not, in general, exactly parallel to the surface. However, it must be remembered that the horizontal scale is considerably expanded with respect to the vertical scale so that the flux lines are nevertheless very nearly parallel to the surface. It is also seen that the flux line spacing, taking into account the difference between the horizontal and vertical scales, is much smaller within the antiferromagnet than in the incident medium (vacuum). This is consistent with a higher power flow intensity within the antiferromagnet, decaying rapidly away from the surface, as shown in the contour plot.

Figure 8(b) shows the energy flux at frequency B, in the bulk region, with power flow in the antiferromagnet perpendicular to the surface, in agreement with the plane wave predictions of Sec. II. It is seen from Fig. 6(b) that, at this frequency, the reflected beam is less intense than the incident beam for all values of x. Thus the net power flow in the vacuum is always to the right. Since there is a slight negative shift of the reflected beam along x, the profile of the overall flux (incident flux minus reflected flux) suffers a positive shift with respect to the incident beam. Flux continuity implies that this shift must also be transferred to the transmitted beam, and this is indeed what is observed in Fig. 8(b). This is qualitatively consistent with a positive shift of the transmitted **E** field as seen in Fig. 7(b).

Although both the **E**-field profile in Fig. 7(b) and the energy intensity profile in Fig. 8(b) show a positive lateral displacement of the transmitted beam, the displacement in Fig. 8(b) is somewhat less than that in Fig. 7(b). This suggests that, within the antiferromagnet, simple examination of the **E**-field distribution does not give a full picture of the beam displacement. In the bulk regions, at which the transmitted power flow is normal to the surface, the magnitude of the time-averaged Poynting vector $\langle S_y\rangle$ is given by $1/2\ \mathrm{Re}(E_zH_x^*)$. In practice, both E_z and H_x are wholly real at these frequencies. A good understanding of the field contributions to the power flow can therefore be gained by comparing $\mathrm{Re}(E_z)$ with $\mathrm{Re}(H_x)$ since $\langle S_y\rangle$ varies as the product of these two quantities. Such a comparison of the transmitted field profiles is presented in Fig. 9(a). It is seen that the two profiles are significantly different. Thus, although the E_z field profile is displaced along the interface in the positive x direction, the H_x field profile is not. In fact, it is slightly displaced in the negative x direction. This explains why the displacement of the transmitted beam, expressed in terms of power flow, is somewhat less than would be predicted from the **E**-field profile.

Figure 8(c) shows the energy flux at frequency C, between the reflection minimum and the lower edge of the reststrahl region. Once again, since this frequency lies within the bulk region, power flow within the antiferromagnet is perpendicular to the surface. The predominant behavior is the same as that observed at frequency B. Thus, for $x\gtrsim -0.08$ cm, there is an overall power flow to the right, laterally displaced in the opposite direction to the displacement of the reflected beam. For $x\lesssim -0.08$ cm, however, the overall power flow is to the left, as shown by the arrows in the lower part of the figure. Note that these arrows are merely indicative of the direction of power flow and were not obtained from a continuation of the flux lines in the upper part of the figure. This behavior is consistent with the profiles of the incident and reflected beams shown in Fig. 6(c) having an incident intensity greater than the reflected intensity for $x\gtrsim -0.08$ cm and a reflected intensity greater than the incident intensity for $x\lesssim -0.08$ cm.

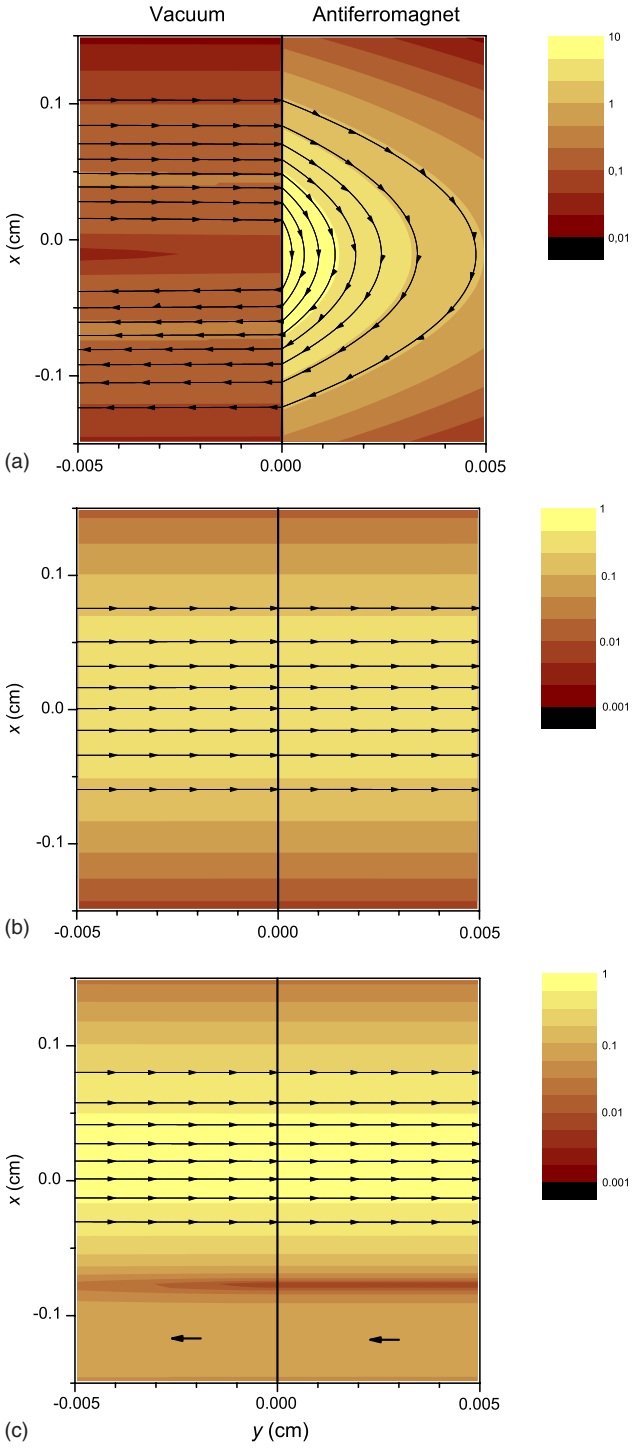

FIG. 8. (Color online) Overall power intensity, normalized with respect to the center of the incident beam, and flux lines in the case of reflection of a normally incident Gaussian beam, of width $g=\lambda$, off a semi-infinite sample of MnF_2 in an external magnetic field of 0.1 T, in the absence of damping. (a) Frequency A (9.0769 cm^{-1}); (b) frequency B (9.0994 cm^{-1}); and (c) frequency C (9.0705 cm^{-1}). The solid vertical black line represents the surface of the sample. Note that, for the sake of clarity, the horizontal scale (y) is expanded with respect to the vertical scale (x). The arrows in the bottom half of (c) are intended only to show the direction of power flow, and were not obtained directly from a continuation of the flux lines.

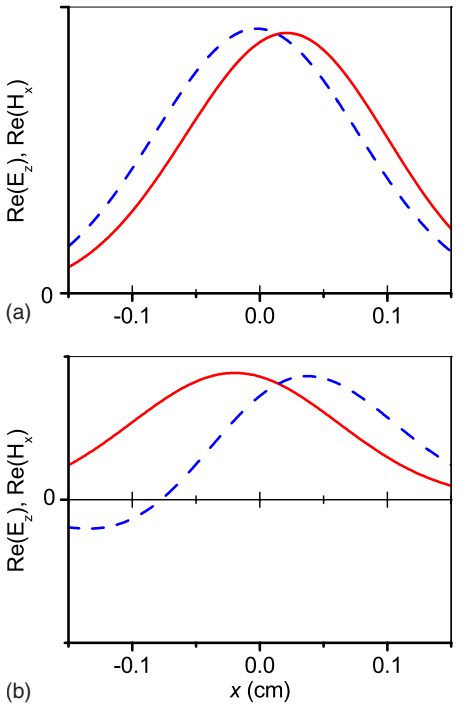

FIG. 9. (Color online) Profiles, along the sample surface, of the real parts of the transmitted E_z (solid red line) and H_x (dashed blue line) fields, in arbitrary units, at bulk region frequencies. (a) Frequency B (9.0994 cm^{-1}); (b) frequency C (9.0705 cm^{-1}). Note that these fields have no imaginary parts.

Comparison of Figs. 8(c) and 7(c) shows that, within the antiferromagnet, the profile of the power flow intensity is now very different from that of the electric field. The latter is displaced in the negative x direction, whereas the former is displaced in the positive x direction, with a small amount of energy returning along $-y$ for $x \lesssim -0.08$ cm. We can once again reconcile this difference by comparing the transmitted E_z and H_x fields. The profiles along x of the real parts of these fields are shown in Fig. 9(b). As before, there are no imaginary parts. We again see that $\mathrm{Re}(E_z)$ profile retains its Gaussian form, and it is always positive. The $\mathrm{Re}(H_x)$ profile is completely different, however, being positive for $x \gtrsim -0.08$ cm and negative for $x \lesssim -0.08$ cm. Since, in the absence of imaginary field components, $\langle S_y \rangle = \frac{1}{2}\mathrm{Re}(E_z)\mathrm{Re}(H_x)$, power flow is to the right when this product is positive and to the left when it is negative, in agreement with the results shown in Fig. 8(c).

One aspect of Fig. 8(c) that requires special attention is that the leftward energy flow shown for $x \lesssim -0.08$ cm appears to be in conflict with the principle of causality since there is no obvious source for this energy and energy flow is strictly normal to the surface at $y=0$ (corresponding to the focal plane of the Gaussian beam). However, if we examine x values close to $x=-0.08$ cm and look several centimeters into the sample (i.e., a large distance from the focal plane), we do find that some flux lines return along the negative y direction for $x \lesssim -0.08$ cm. This is seen from Fig. 10, which shows power flow in the antiferromagnet within a narrow x range but extending to large y. This figure thus confirms that the leftward energy flow seen in Fig. 8 does not violate any

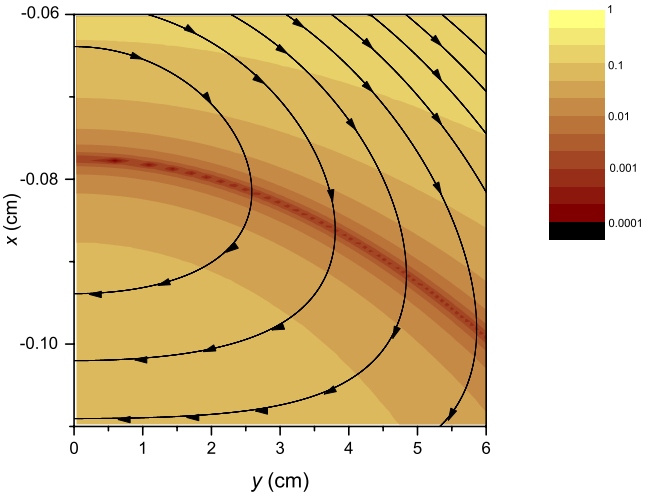

FIG. 10. (Color online) Details of power intensity and flux lines close to $x=-0.08$ cm within a semi-infinite sample of MnF_2 in the case of the reflection shown in Fig. 8(c). In this figure, the vertical scale (x) is expanded with respect to the horizontal scale (y).

energy conservation principles. Note that the integrals used in the calculation of Fig. 10 had limits of $\pm 10k_0$ (as opposed to $\pm k_0$ used in the other calculations) in order to avoid spurious effects associated with truncation of the integral.

We finally examine how the inclusion of damping affects the analysis. Figure 11 shows energy flow in the presence of damping for all three frequencies. We have not attempted to follow the flux lines since there is now no flux continuity. The length of the energy flow arrows is, however, intended to indicate the power flow intensity on a logarithmic scale.

Figure 11(a) shows the power flow at frequency A in the reststrahl region. The power flow is similar to that seen without damping, but we now see that, within the antiferromagnet, the direction of power flow is no longer along the contour lines. Overall there is less power returning along the $-y$ direction than in the undamped case. Nevertheless, there is overall power flow to the left for $x \lesssim -0.03$ cm, as expected from Fig. 6. It must be remembered, however, that MnF_2 has extremely low damping in comparison with most systems, and in other systems it is likely that there will be no overall leftward energy flow at any x value.

At frequency B, shown in Fig. 11(b), the behavior is almost identical to that seen in Fig. 8(b) with no damping present. This frequency is sufficiently distant from the resonance frequency for damping to be unimportant.

The situation at frequency C in the presence of damping [Fig. 11(c)] is noticeably different from the undamped case [Fig. 8(c)]. The power transmitted into the antiferromagnet is no longer perpendicular to the surface. One effect of this is that there can be an overall power flow to the left at the bottom part of the figure without the need for the large penetration into the antiferromagnet that occurs for zero damping (Fig. 10). The overall behavior is now very similar to that in the reststrahl region, with the distinction between the bulk and reststrahl regions being ill defined in the presence of damping.

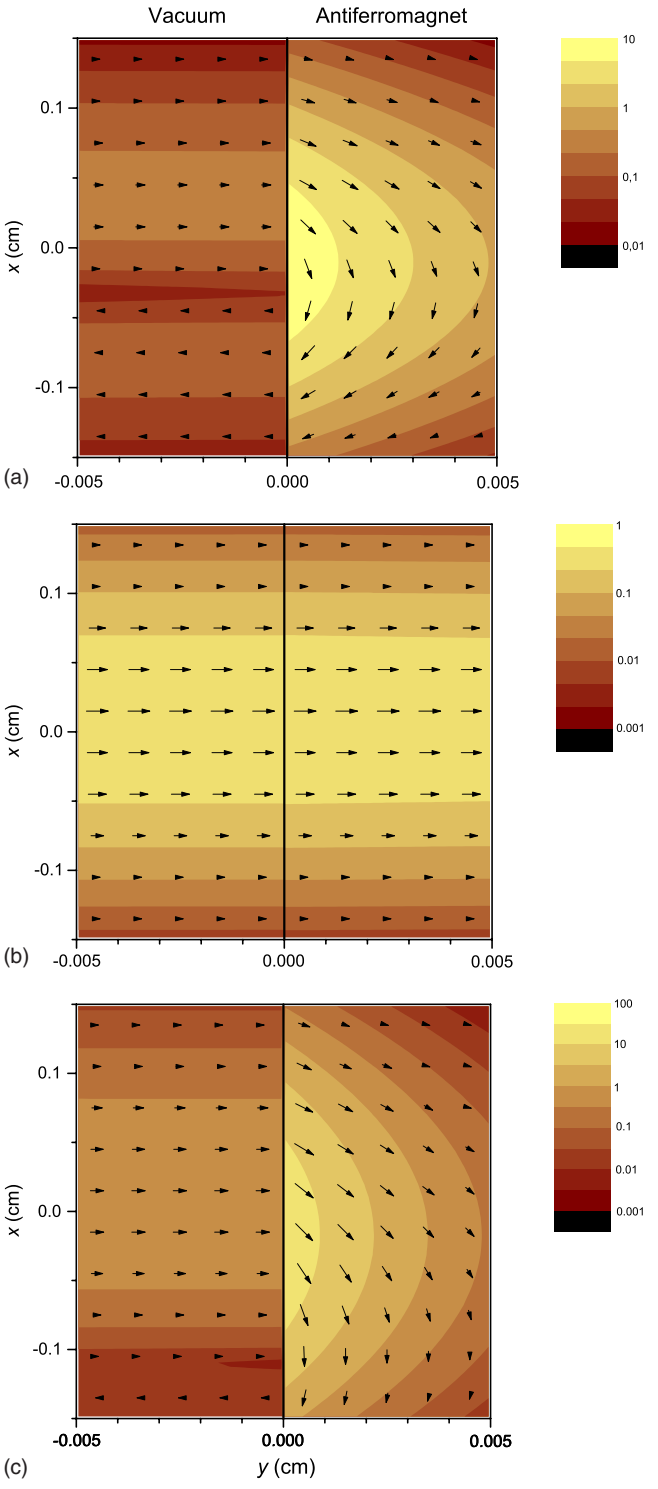

FIG. 11. (Color online) Overall power intensity and direction in the case of reflection of a normally incident Gaussian beam, of width $g=\lambda$, off a semi-infinite sample of MnF_2 in an external magnetic field of 0.1 T, with $\Gamma=0.0007$ cm^{-1}. (a) Frequency A (9.0769 cm^{-1}); (b) frequency B (9.0994 cm^{-1}); and (c) frequency C (9.0705 cm^{-1}). The solid vertical black line represents the surface of the sample. Note that, for the sake of clarity, the horizontal scale (y) is expanded with respect to the vertical scale (x).

VI. CONCLUSIONS

The above analysis shows that power flow upon reflection of a normally incident beam off an antiferromagnet is consistent with the plane wave result, which gives power flow parallel to the surface in the reststrahl regions and normal to the surface in the bulk regions. A lateral displacement of the reflected beam is possible in either region. In the reststrahl regions, this displacement is in the direction of power flow along the interface and can be anticipated using power conservation principles. In the bulk regions a displacement of the transmitted beam, in the direction opposite to that of the reflected beam, is necessary to ensure flux continuity. The unusual energy flow behavior found, in the absence of damping, between the reflection minimum and the bottom of the reststrahl region (represented here by frequency C) does not appear ultimately to violate any energy conservation principles. However, the situation is somewhat more straightforward in the presence of damping, and the power flow is in this case similar to that in the reststrahl regions.

Although the analysis has been performed in the case of reflection off an antiferromagnet, it should be noted that the unusual behavior described in this paper is due to the form of the permeability tensor in Eq. (1). In principle, the same type of behavior could also be expected in other materials such as ferromagnets, which also have a gyromagnetic permeability of this form.

ACKNOWLEDGMENT

This work was partially financed by the Brazilian Research Agency CNPq (Projects Universal No. 482238/2007-0, No. CT-ENERG 554889/2006-4, and No. CNPq-Rede NanoBioestruturas 555183/2005-0).

*Corresponding author; tdumelow@yahoo.com.br
†Address for correspondence.

[1] F. Goos and H. Hänchen, Ann. Phys. **436**, 333 (1947).
[2] H. K. V. Lotsch, Optik (Stuttgart) **32**, 116 (1970); **32**, 189 (1970); **32**, 299 (1970); **32**, 553 (1970).
[3] W. J. Wild and C. L. Giles, Phys. Rev. A **25**, 2099 (1982).
[4] P. T. Leung, Z. W. Chen, and H.-P. Chiang, Opt. Commun. **276**, 206 (2007).
[5] M. Merano, A. Aiello, G. W. 't Hooft, M. P. van Exter, E. R. Eliel, and J. P. Woerdman, Opt. Express **15**, 15928 (2007).
[6] H. M. Lai and S. W. Chan, Opt. Lett. **27**, 680 (2002).
[7] N.-H. Shen, J. Chen, Q.-Y. Wu, T. Lan, Y.-X. Fan, and H.-T. Wang, Opt. Express **14**, 10574 (2006).
[8] J. B. Götte, A. Aiello, and J. P. Woerdman, Opt. Express **16**, 3961 (2008).
[9] J. He, J. Yi, and S. He, Opt. Express **14**, 3024 (2006).
[10] F. Lima, T. Dumelow, J. A. P. da Costa, and E. L. Albuquerque, Europhys. Lett. **83**, 17003 (2008).
[11] H. K. V. Lotsch, J. Opt. Soc. Am. **58**, 551 (1968).
[12] H. Kogelnik and H. P. Weber, J. Opt. Soc. Am. **64**, 174 (1974).
[13] A. W. Snyder and J. D. Love, Appl. Opt. **15**, 236 (1976).
[14] J. L. Agudín, Phys. Rev. **171**, 1385 (1968).
[15] K. Artmann, Ann. Phys. **437**, 87 (1948).
[16] B. R. Horowitz and T. Tamir, J. Opt. Soc. Am. **61**, 586 (1971).
[17] M. McGuirk and C. K. Carniglia, J. Opt. Soc. Am. **67**, 103 (1977).
[18] R. H. Renard, J. Opt. Soc. Am. **54**, 1190 (1964).
[19] H. M. Lai, C. W. Kwok, Y. W. Loo, and B. Y. Xu, Phys. Rev. E **62**, 7330 (2000).
[20] T. Dumelow, R. E. Camley, Kamsul Abraha, and D. R. Tilley, Phys. Rev. B **58**, 897 (1998).
[21] D. L. Mills and E. Burstein, Rep. Prog. Phys. **37**, 817 (1974).
[22] Kamsul Abraha and D. R. Tilley, Surf. Sci. Rep. **24**, 129 (1996).
[23] L. D. Landau and L. P. Lifshitz, *Electrodynamics of Continuous Media*, 2nd ed. (Pergamon, Oxford, 1984).
[24] T. Dumelow and M. C. Oliveros, Phys. Rev. B **55**, 994 (1997).
[25] X. Chen and C.-F. Li, Phys. Rev. E **69**, 066617 (2004).